PAPER

Check for updates

Tungsten regulated medium-entropy heterostructure as a highly efficient electrocatalyst for oxygen evolution reaction†

Jianliang Yuan,[a,d] Qianglong Qi, [iD] [a,b] Qingwen Wan,[a,b] Jiangli Gong,[a,d] Yue Zhang,[a,b] Yuebin Feng,[c] Chengxu Zhang [iD] *[a] and Jue Hu [iD] *[a,b]

Medium-entropy alloys (MEAs) as electrocatalysts have attracted considerable attention in the field of water splitting. However, effective modulation of MEAs to achieve highly efficient catalysis remains a challenge. Herein, we applied a metal–organic framework (MOF) templating strategy to obtain FeCoNi MEA nanoparticles with excellent oxygen evolution reaction (OER) activity and tungsten improved FeCoNi-W medium-entropy heterostructure catalysts. The incorporation of tungsten changes the electronic structure of FeCoNi MEA. The mesoporous alloy exhibits multiple active sites and unique atomic-level synergies that enhance the effective binding of reactants and the formation of crucial *OH intermediates critical for OER. The rationally designed and constructed tungsten-refined FeCoNi-W medium-entropy heterostructure electrode demonstrates superior OER performance (270 mV at 10 mA cm^{-2}, a Tafel slope of 43.2 mV dec^{-1}) and stability (50 h at 100 mA cm^{-2}) compared to commercial noble metal electrodes. This work will provide a basis for tailoring the properties of medium/high-entropy alloys (M/HEAs) through local chemical modification.

1 Introduction

Hydrogen energy, as a highly potent clean energy source, is gradually becoming a crucial component of the future energy system.[1,2] Through water splitting reactions, we can efficiently produce hydrogen energy by utilizing renewable resources.[3–5] However, a major challenge is the oxygen evolution reaction (OER), a crucial step in water splitting.[6] The OER involves a 4e$^-$ transfer process that has sluggish kinetics and a high energy barrier, resulting in a significant overpotential.[7] Although noble metal-based electrocatalysts (such as RuO$_2$/IrO$_2$) have been proven to effectively accelerate the OER process,[8] their high costs, limited availability, and instability severely hinder their large-scale application. They exhibit various advantageous properties such as high yield strength,[9] thermal stability,[10] corrosion resistance,[11] notable magnetic characteristics,[12] and superior catalytic activity. Recently,

medium-entropy alloys (MEAs) have demonstrated significant advantages in electrochemical stability, elemental diversity, and synergistic effects in catalytic applications due to their unique four core effects, providing a new pathway to replace or reduce the use of noble metals.[13–17] Typically, the catalytic performance of MEAs can be effectively enhanced by designing nanostructured morphologies and incorporating multi-element doping.[18,19] These methods not only increase the number of reactive active sites, but also improve their inherent catalytic properties. Notably, incorporating high-valent metal elements into metal oxide electrocatalysts can optimize the OER performance by adjusting the three-dimensional metal oxide redox energy landscape.[20] For instance, Sargent and colleagues reported an FeCoMoW oxide electrocatalyst that outperformed FeCo oxide catalysts.[21] Furthermore, they developed an FeCoW hydroxide catalyst that could stably operate at a moderate overpotential for approximately 500 hours under 1 M KOH conditions.[22] These studies suggest that incorporating multiple metal elements into MEAs can finely tune the electronic structure and provide diverse metal active sites. However, the thermodynamic immiscibility between these elements often leads to phase separation and composition segregation, thereby reducing the overall performance. Therefore, designing suitable medium-entropy structures and selecting appropriate preparation methods become crucial. In recent years, significant progress has been made in the controlled

[a]*Faculty of Metallurgical and Energy Engineering, Kunming University of Science and Technology, Kunming, China. E-mail: chxzhang@kust.edu.cn, hujue@kust.edu.cn*
[b]*Key Laboratory of Unconventional Metallurgy, Kunming University of Science and Technology, Kunming, Yunnan, China*
[c]*Faculty of Science, Kunming University of Science and Technology, Kunming, China*
[d]*LuXi KuoBo Precious Metals Co. Ltd., Honghe, Yunnan, China*
†Electronic supplementary information (ESI) available. See DOI: https://doi.org/10.1039/d5dt00258c

synthesis and innovative design of FeCoNi-based nanocatalysts, advancing the research on electrocatalytic materials and broadening their application fields.[23–25] Meanwhile, given the inherent functional characteristics of interfacial structures in catalysis, numerous studies have focused on electrocatalyst nanomaterials developed through interfacial engineering.[26] The internal electric fields at the epitaxial interfaces in these materials significantly enhance the electrocatalytic performance, promoting hydrogen adsorption and accelerating electron transfer.

Here, we synthesized a nano-heterojunction catalyst rich in rare earth elements Fe, Co, Ni, and W using a simple hydrothermal method. By precisely controlling the equimolar ratio of transition metal elements, we achieved high electrocatalytic performance for FeCoNi-W. The prepared electrocatalysts exhibited excellent catalytic performance, benefiting from abundant active sites, multi-element synergistic effects, and entropy stability. In particular, we rationally designed and constructed a tungsten-refined FeCoNi-W medium-entropy heterostructure electrode that surpassed the FeCoNi MEA electrode in terms of OER performance and stability (achieving an overpotential of 270 mV at 10 mA cm^{-2} with a high turnover frequency and stable operation for 50 hours at 100 mA cm^{-2}). This superior performance is attributed to the addition of tungsten, which alloyed FeCoNi with the less electronegative W element, forming a unique medium-entropy heterostructure. This process fine-tunes the surface electronic states of the active metal centers, facilitating the adsorption of OH and enhancing the effective binding of reactants. This study provides a simple and effective method for synthesizing heterogeneous materials containing nanoscale multi-metal elements, providing new vitality into the development of the hydrogen energy field.

2　Results and discussion

The FeCoNi-W medium-entropy alloy-oxide (MEA/MEO) heterostructure electrocatalyst was synthesized using a tungsten (W) modulation strategy. FeCoNi and FeCoNiW metal–organic frameworks (MOFs) were synthesized using a solvothermal method as reported in the literature. Following this, nanoalloy catalysts were fabricated through high-temperature reduction in an H$_2$/Ar environment. Scheme S1† depicts the preparation process of the FeCoNi-W MEA/MEO heterostructure catalyst. As shown in Fig. 1a, the two prepared catalysts exhibited excellent crystallinity; the X-ray diffraction (XRD) pattern of the FeCoNi MEA nanoparticles showed no detectable peak of metal oxides. In particular, the peak located at approximately 44° in the FeCoNi sample corresponds to the (111) plane of the FCC structure (FeNi$_3$, PDF# 38-0419). Notably, the peak positions in the FeCoNi sample exhibit slight shifts, indicating the successful incorporation of these elements into the nanocatalyst, forming the MEA structure. Additionally, compared to FeCoNi/C, the FeCoNi-W XRD exhibited clear peaks of metal oxides at 24.3° and 30.3°. These peaks highly matched the (110) and (111) planes of the FeWO$_4$ phase (PDF# 74-1100), indicating the formation of the FeCoNi-W medium-entropy alloy/oxide (MEA/MEO) heterostructure. Fig. 1b displays the Raman spectra of FeCoNi and FeCoNi-W, with characteristic peaks at 1350 and 1582 cm^{-1} representing the D and G bands of carbon-based materials, respectively. Both D and G peaks are Raman signatures for carbon atom crystals. Specifically, the D peak indicates the presence of defects in the carbon atom crystal; the G peak signifies the stretching vibration of sp^2 hybridized carbon atoms within the plane.[27] In carbon-based materials, the ratio of the intensities of the D and G peaks (I_D/I_G) serves as an indication of lattice defects and material disorder. The I_D/I_G ratio for FeCoNi was 0.76, suggesting a relatively intact crystal structure. However, upon the introduction of W into the FeCoNi matrix, the I_D/I_G ratio increased to 0.88, indicating a higher degree of lattice defects and oxygen-containing functional groups in FeCoNi-W. This increase led to an enhanced level of disorder within the material.

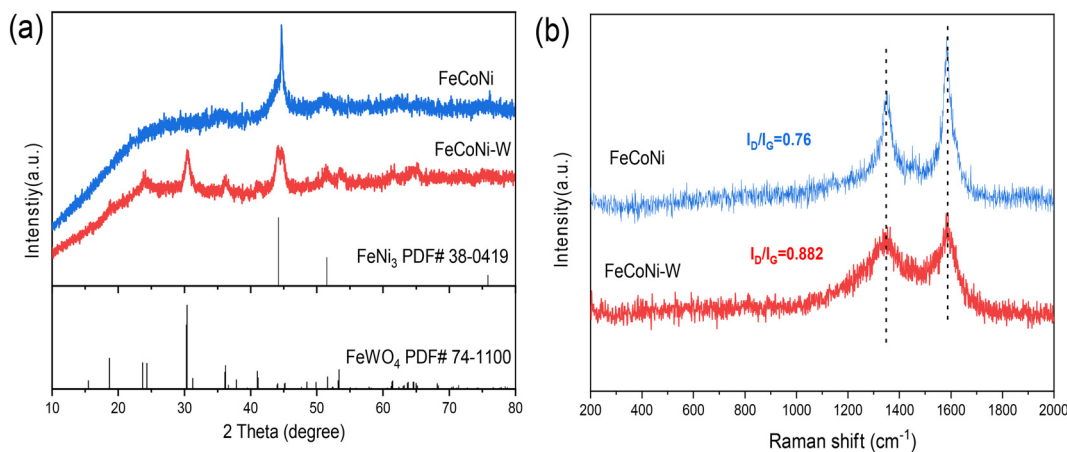A detailed investigation of the microstructure and morphology of the catalysts was conducted using transmission

Fig. 1 (a) XRD patterns and (b) Raman spectra of FeCoNi MEA and FeCoNi-W medium-entropy heterostructures.

electron microscopy (TEM) and scanning electron microscopy (SEM). The FeCoNi and FeCoNi-W medium-entropy heterostructure samples exhibit similar morphological characteristics, consisting of aggregated particles formed by the stacking of irregularly surfaced nanoparticles (Fig. 2a, b and Fig. S1†). To gain a deeper understanding of the microstructure of these samples, High-Resolution TEM (HR-TEM) was employed. The HR-TEM images of FeCoNi-W presented in Fig. 2c and d clearly reveal the abundant presence of $FeWO_4$ nanoparticles on the surfaces and edges of the FeCoNi nanospheres. In Fig. 2e, lattice fringes with spacings of approximately 2.94 Å (yellow lines) and 2.06 Å (red lines) were observed, which are attributed to the (111) plane of medium-entropy oxides within the medium-entropy heterostructure

nanocatalyst and the (111) diffraction peak of the FeCoNi alloy nanocatalyst, respectively. Notably, the combination of $FeWO_4$ and FeCoNi forms a unique heterogeneous structure, resulting in a shift in the peak position of $FeWO_4$ (111) compared to pure FeCoNi. To gain insights into the elemental distribution of FeCoNi-W, energy-dispersive X-ray (EDX) mapping analysis was performed. The EDX Spectroscopy elemental mapping results of the FeCoNi-W sample show a uniform distribution of five elements within the sample, further confirming the successful synthesis of the FeCoNi-W heterogeneous structure (Fig. 2f and Fig. S2†).

X-ray photoelectron spectroscopy (XPS) characterization and analysis were performed to investigate in detail the surface chemical states and chemical structures of the prepared
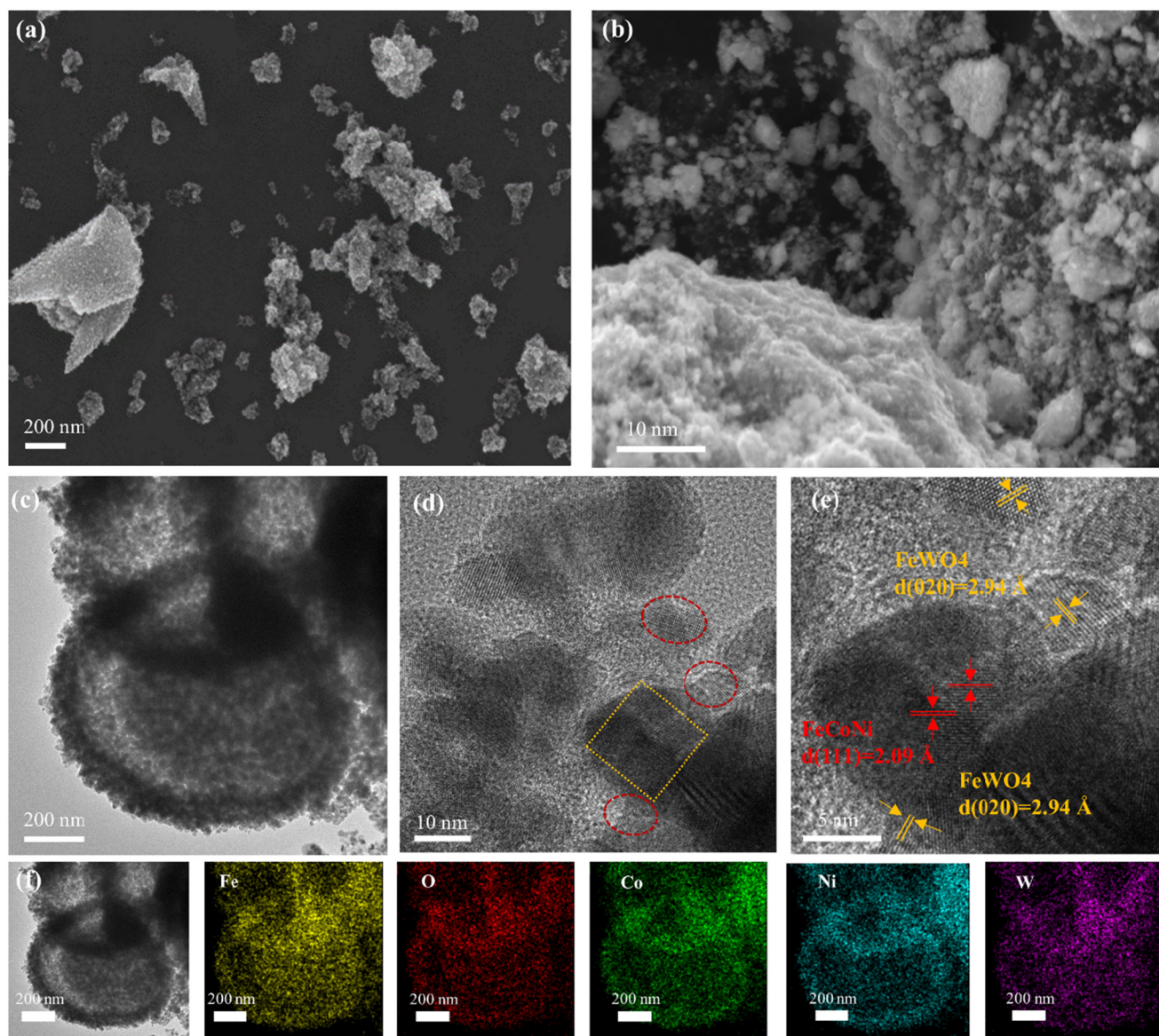

Fig. 2 Morphological characterization of FeCoNi-W. SEM images of (a) FeCoNi and (b) FeCoNi-W. (c) TEM and HR-TEM images provide further insights into the microstructure of FeCoNi-W. (d) An enlarged TEM image is shown in (e). (f) Elemental mapping of FeCoNi-W highlights the distribution of the corresponding elements.
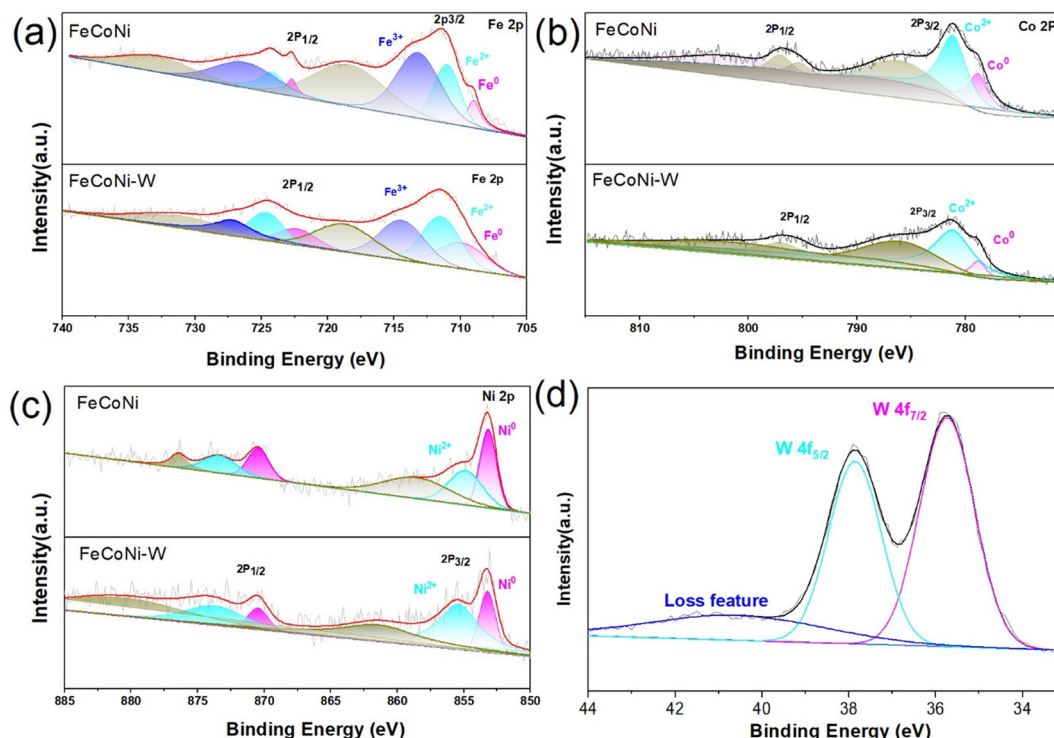
Fig. 3 High-resolution XPS spectra of FeCoNi-W. (a) Fe 2p spectra of FeCoNi-W and FeCoNi. (b) Co 2p spectra of FeCoNi-W and FeCoNi. (c) Ni 2p spectra of FeCoNi-W and FeCoNi. (d) W 4f spectrum of FeCoNi-W.

FeCoNi MEA and the alloyed FeCoNi-W MEA/MEO catalyst with a heterogeneous compound formed by incorporating the less electronegative element W. As shown in Fig. S3,† the XPS spectra of both FeCoNi MEA and FeCoNi-W MEA/MEO show the presence of the same constituents, with a distinct peak for element W in FeCoNi-W MEA/MEO clearly visible. In addition, peak matching was performed on the high-resolution XPS spectra of the primary constituents of the FeCoNi MEA and FeCoNi-W MEA/MEO catalysts. The Fe 2p high-resolution spectrum (Fig. 3a) exhibits two peaks at 710.8 eV and 724.91 eV, corresponding to Fe^{2+} $2p_{3/2}$ and Fe^{2+} $2p_{1/2}$, respectively, while peaks at 713.6 eV and 727.48 eV are associated with Fe^{3+} in the catalyst material. The peaks located at 709.08 eV and 723.23 eV represent metallic Fe, and those at 716.7 eV and 734.07 eV are satellite peaks.[28] Furthermore, surface oxidation of alloy particles leads to the formation of high-valent iron. Compared with the FeCoNi MEA sample, the binding energy of the Fe $2p_{3/2}$ peak in the FeCoNi-W MEA/MEO catalyst exhibits a positive shift (to 707.3 eV), indicating that the incorporation of the less electronegative W element reduces the electron cloud density around Fe atoms, effectively "pulling away" or "depleting" electrons, thereby causing a positive shift in the binding energy of the Fe $2p_{3/2}$ peak. This alteration in the electronic structure may influence the catalytic performance of the FeCoNi-W catalyst. As a heterophase element, W possesses a different atomic radius and electron configuration compared to Fe, Co, and Ni, disrupting the original electronic balance and causing a redistribution of electrons around Fe atoms

when the W heterophase is formed in the alloy. Analysis of the high-resolution Ni XPS spectrum reveals two prominent peaks in the Ni $2p_{3/2}$ region of the FeCoNi-W catalyst: the peak at 853.2 eV corresponds to metallic Ni^0,[29] while the peak at 856.9 eV is attributed to Ni^{2+}, indicating partial oxidation on the catalyst surface. Notably, the introduction of the less electronegative W element to form an alloy/oxide heterogeneous junction results in a slight negative shift in the binding energy of metallic Ni. Additionally, in the spectrum of FeCoNi, the peaks at 781.0 eV and 796.7 eV correspond to the $2p_{3/2}$ and $2p_{1/2}$ energy levels of metallic Co, respectively (Fig. 3b).[30,31] Analysis of the high-resolution Co XPS spectrum reveals two prominent peaks in the Co $2p_{3/2}$ region of the FeCoNi-W catalyst: the peak at 778.8 eV corresponds to metallic Co^0, while the peak at 781.1 eV is attributed to Co^{2+}, indicating partial oxidation on the catalyst surface. For the FeCoNi-W catalyst, the peaks at 853.2 eV and 870.4 eV belong to the $2p_{3/2}$ and $2p_{1/2}$ energy levels of metallic Ni^0, respectively (Fig. 3c). It is worth noting that the incorporation of the less electronegative W element into the FeCoNi alloy results in varying degrees of binding energy shifts for Fe^0, Co^0, and Ni^0. This phenomenon reveals a significant synergistic electronic coupling effect among Fe, Co, Ni, and W atoms (Fig. 3d), which may alter the adsorption behavior of OER intermediates on Co, Ni, and Fe sites.[32] This discovery further confirms the existence of synergistic electronic coupling among Fe, Co, Ni, and W atoms.

The OER catalytic activity was investigated in a 1.0 M KOH electrolyte employing a standard three-electrode setup.
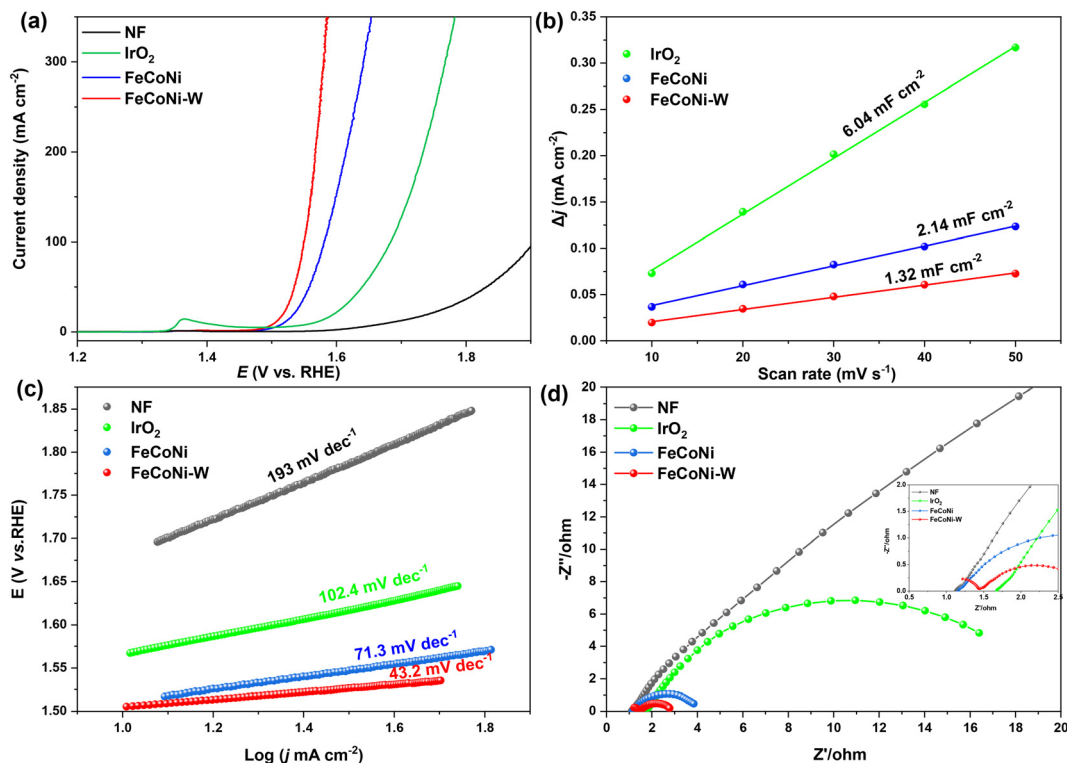
Fig. 4 (a) LSV curves of FeCoNi MEA, FeCoNi-W MEA/MEO heterostructure nanocatalyst, and IrO₂ catalysts; (b) ECSA curves represented by the values of electrochemical C_{dl} of FeCoNi, FeCoNi-W, and IrO₂ catalysts. (c) Tafel slope of FeCoNi, FeCoNi-W, and IrO₂ catalysts; (d) EIS plots with fitting lines of FeCoNi, FeCoNi-W, and IrO₂ catalysts at a voltage of 1.53 V $vs.$ RHE.
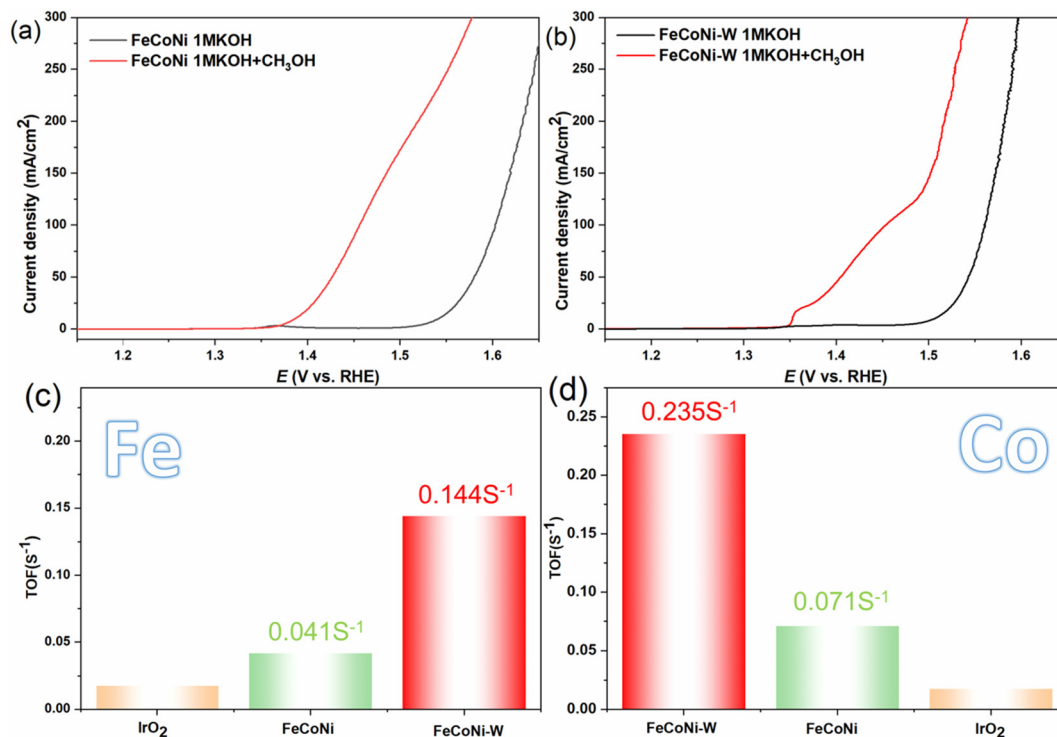

Fig. 5 Linear sweep voltammetry curves of (a) FeCoNi MEA and (b) FeCoNi-W loaded in 1.0 M KOH with and without methanol (0.602 mol L⁻¹). (c) TOF diagram of Fe in commercial IrO₂ and FeCoNi and FeCoNi-W catalysts. (d) TOF diagram of Co in commercial IrO₂ and FeCoNi and FeCoNi-W catalysts.

Subsequently, the electrocatalytic OER activities of FeCoNi MEA and FeCoNi-W MEA/MEO heterostructure nanocatalysts were then compared using cyclic voltammetry (CV) at a scan rate of 0.005 V s^{-1}. The results revealed that the FeCoNi-W heterostructure nanocatalyst exhibited superior performance (Fig. 4a). Notably, the constructed medium-entropy heterogeneous structured electrode of tungsten-refined FeCoNi-W exhibits superior OER performance. At a current density of 10 mA cm^{-2}, the alloying of the less electronegative W element results in the formation of a unique FeCoNi-W medium-entropy alloy/oxide heterogeneous junction catalyst, exhibiting an overpotential of only 270 mV. This is 18.2 mV lower than the overpotential of the FeCoNi MEA. By analyzing the CV curves in the double-layer region at various scan rates (Fig. 4b), the double-layer capacitance (C_{dl}), which is positively correlated with ESCA, was determined. The heterojunction catalyst obtained after incorporating the less electronegative W element exhibited a higher C_{dl} value (2.14 mF cm^{-2} for FeCoNi-W vs. 1.23 mF cm^{-2} for FeCoNi) compared to the pure FeCoNi MEA. Moreover, FeCoNi-W possessed the lowest Tafel slope (43.2 mV dec^{-1}) (Fig. 4c), indicating that the heterojunction catalyst, with the incorporation of the less electronegative W element, demonstrated faster kinetics during the OER. Furthermore, electrochemical impedance spectroscopy (EIS) was employed to gain insights into the interfacial transport mechanisms of the electrocatalyst. In contrast, the FeCoNi-W MEA/MEO heterostructure nanocatalyst exhibits a lower charge transfer resistance, indicating a superior charge transfer rate during the OER process (Fig. 4d).

As shown in Fig. 5a, b and Fig. S4, S5,† the methanol oxidation reaction (MOR) is employed as an effective method to evaluate the adsorption of OER intermediates, where the increase in current density positively correlates with the coverage of the catalytic reaction intermediate OH*. The results indicate that the FeCoNi-W MEA/MEO heterostructure nanocatalyst exhibits a notably higher current density compared to FeCoNi MEA,
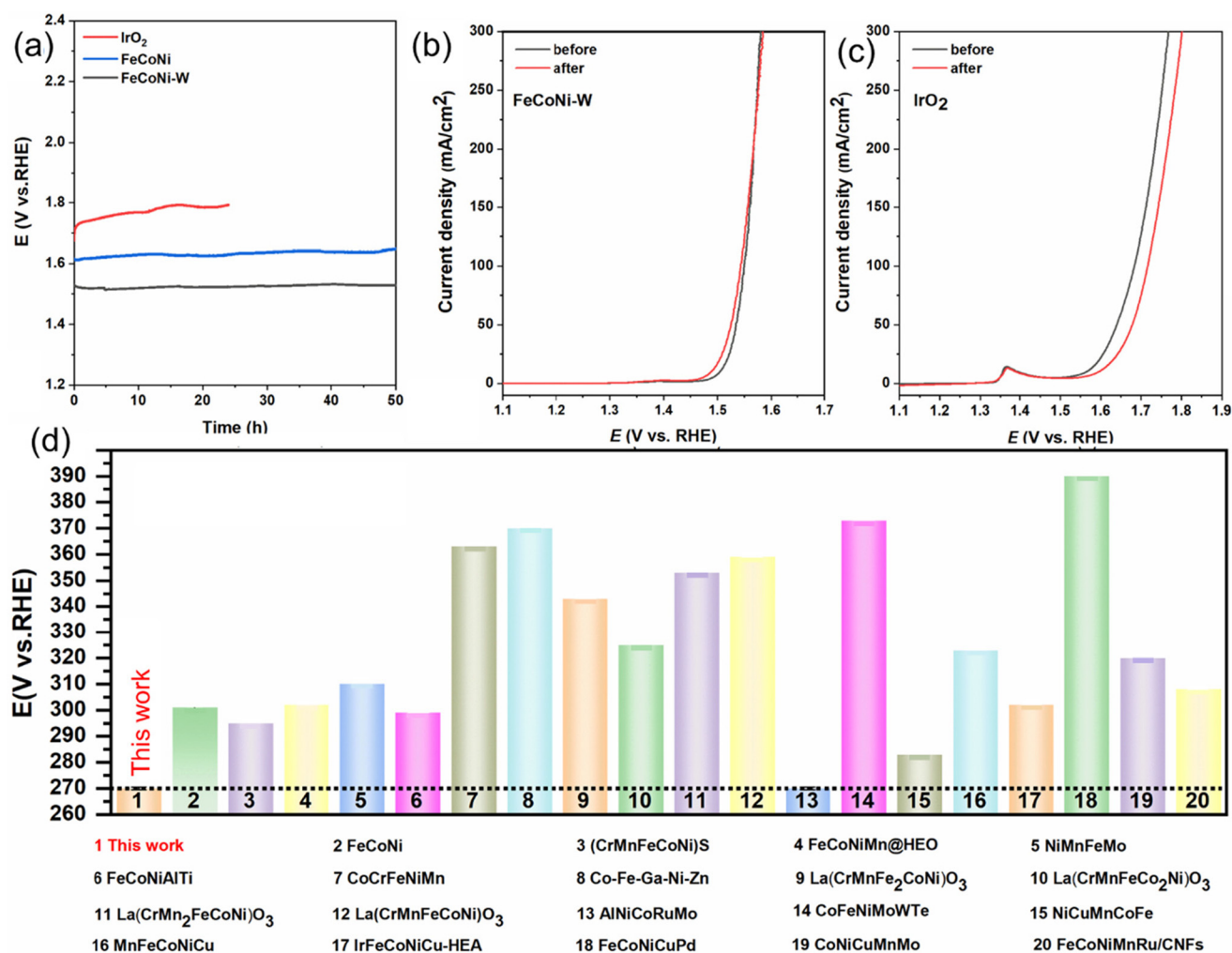

Fig. 6 Electrocatalytic stability of FeCoNi-W. (a) The polarization curves of FeCoNi-W before and after a 50 hours stability test at 100 mA cm^{-2} illustrate its durability. (b) For comparison, the polarization curves of IrO$_2$ before and after the same test are presented. (c) The time−potential (E−t) curves of IrO$_2$, FeCoNi, FeCoNi-W, and commercial IrO$_2$ catalysts demonstrate their stability over time. (d) The FeCoNi-W catalyst exhibits comparable or superior performance to recently reported high-entropy OER catalysts in 1.0 M KOH at a current density of 10 mA cm^{-2}.

suggesting that the formation of heterogeneous interfaces effectively modulates the adsorption of the intermediate OH* in the FeCoNi-W MEA/MEO heterostructure nanocatalyst.[33] Additionally, the turnover frequency (TOF) of the FeCoNi MEA, FeCoNi-W MEA/MEO heterostructure nanocatalyst was evaluated to assess its intrinsic activity at a constant overpotential of 300 mV (Fig. 5c and d). The TOF values for Fe and Co in the FeCoNi catalyst are 0.041 s^{-1} and 0.071 s^{-1}, respectively. However, in the FeCoNi-W catalyst, the TOF values for Fe and Co are significantly higher, at 0.144 s^{-1} and 0.235 s^{-1}, respectively, representing a 2–3 times increase in intrinsic activity compared to the FeCoNi catalyst. Electrocatalysts, serving as pivotal materials in electrochemical reactions, have their performance directly influencing the efficiency and sustainability of these reactions. During extended periods of use, particularly under high current density operating conditions, the durability of electrocatalysts emerges as one of the crucial indicators for assessing their performance quality. To further investigate the stability of FeCoNi MEA and FeCoNi-W MEA/MEO heterostructure nanocatalysts, we conducted chronopotentiometry experiments. The long-term stability of the FeCoNi-W MEA/MEO heterostructure nanocatalyst material was evaluated through chronopotentiometry (E–t) tests conducted over 50 hours at a constant current density of 100 mA cm^{-2}. As shown in Fig. 6a, after 50 hours of stability testing, the FeCoNi-W material exhibited excellent stability at 10 mA cm^{-2}, with only a slight increase in overpotential of a few millivolts at a current density of 100 mA cm^{-2}, a trend that is significantly superior to that of IrO_2 (Fig. 6b and c). Notably, the performance of the FeCoNi-W electrode surpasses many previously reported OER catalysts, such as polymetallic alloys, polymetallic (oxygen) hydroxides,[34,35] oxides,[36] sulfides,[37] and noble metal alloys (Fig. 6d and Tables S1 and S2†).[38]

3 Conclusion

In summary, the tungsten-refined FeCoNi-W medium-entropy heterostructure catalyst was prepared through a sacrificial MOF templating method. Compared to the FeCoNi MEA electrode, the rationally designed and constructed tungsten-refined FeCoNi-W medium-entropy heterostructure electrode exhibits superior oxygen evolution reaction (OER) performance (270 mV at 10 mA cm^{-2}, which is 18 mV lower than that of pure FeCoNi MEA) and stability (stable operation for 50 hours at 100 mA cm^{-2}). This is attributed to the incorporation of tungsten metal, which alloys FeCoNi with the less electronegative W element to form a unique medium-entropy heterostructure. Experiments such as methanol probing have revealed that the alloying of the less electronegative W element with Fe, Co, and Ni, which have large differences in atomic radii, finely tunes the surface electronic states of the active metal centers, facilitating the adsorption of OH and enhancing the effective binding of reactants. The rational design of heterostructure nanoparticles proposed in this study provides a foundation for designing a new generation of M/HEA nanomaterials with efficient catalytic oxygen evolution.

Data availability

The data that have been used are confidential.

Conflicts of interest

We declare that we have no financial and personal relationships with other individuals or organizations that could inappropriately influence our work.

Acknowledgements

References

1 J. Hu, C. Zhang, P. Yang, J. Xiao, T. Deng, Z. Liu, B. Huang, M. K. H. Leung and S. Yang, *Adv. Funct. Mater.*, 2019, **30**, 1908520.

2 Q. Qi, J. Hu, S. Guo, H. Song, S. Wang, Y. Yao, T. Le, W. Li, C. Zhang and L. Zhang, *Appl. Catal., B*, 2021, **299**, 120637.

3 J. Hu, C. Zhang, L. Jiang, H. Lin, Y. An, D. Zhou, M. K. H. Leung and S. Yang, *Joule*, 2017, **1**, 383–393.

4 J. Hu, C. Zhang, Y. Zhang, B. Yang, Q. Qi, M. Sun, F. Zi, M. K. H. Leung and B. Huang, *Small*, 2020, **16**, 202002212.

5 H. Liu, H. Dong, L. Fu, G. Lin, G. Zhang, S. Wang and L. Zhang, *Chem. Eng. J.*, 2023, **467**, 143493.

6 H. Zhu, S. Sun, J. Hao, Z. Zhuang, S. Zhang, T. Wang, Q. Kang, S. Lu, X. Wang, F. Lai, T. Liu, G. Gao, M. Du and D. Wang, *Energy Environ. Sci.*, 2023, **16**, 619–628.

7 K. Zhang and R. Zou, *Small*, 2021, **17**, 1613–6810.

8 Y. Zhang, C. Zhang, Y. Mei, T. Le, H. Shao, H. Jiang, Y. Feng and J. Hu, *Int. J. Hydrogen Energy*, 2022, **47**, 36831–36842.

9 K. Zhou, Z. Wang, Z. Chai, Y. Jia, C. Zhu, L. Xia, J. Li and J. Wang, *Mater. Sci. Eng., A*, 2022, **840**, 142856.

10 H. W. Deng, Z. M. Xie, M. M. Wang, Y. Chen, R. Liu, J. F. Yang, T. Zhang, X. P. Wang, Q. F. Fang, C. S. Liu and Y. Xiong, *Mater. Sci. Eng., A*, 2020, **774**, 138925.

11 S. Shuang, G. J. Lyu, D. Chung, X. Z. Wang, X. Gao, H. H. Mao, W. P. Li, Q. F. He, B. S. Guo, X. Y. Zhong, Y. J. Wang and Y. Yang, *J. Mater. Sci. Technol.*, 2023, **139**, 59–68.

12 Z.-J. Chen, T. Zhang, X.-Y. Gao, Y.-J. Huang, X.-H. Qin, Y.-F. Wang, K. Zhao, X. Peng, C. Zhang, L. Liu, M.-H. Zeng and H.-B. Yu, *Adv. Mater.*, 2021, **33**, 202101845.

13 D. H. Chung, X. D. Liu and Y. Yang, *J. Alloys Compd.*, 2020, **846**, 156189.

14 B. Gludovatz, A. Hohenwarter, K. V. S. Thurston, H. Bei, Z. Wu, E. P. George and R. O. Ritchie, *Nat. Commun.*, 2016, **7**, 10602.

15 C.-Y. Hsu, C.-C. Juan, T.-S. Sheu, S.-K. Chen and J.-W. Yeh, *JOM*, 2013, **65**, 1840–1847.

16 C. W. Lin, M. H. Tsai, C. W. Tsai, J. W. Yeh and S. K. Chen, *Mater. Sci. Technol.*, 2015, **31**, 1165–1170.

17 W.-L. Hsu, C.-W. Tsai, A.-C. Yeh and J.-W. Yeh, *Nat. Rev. Chem.*, 2024, **8**, 471–485.

18 J. W. Bae, J. B. Seol, J. Moon, S. S. Sohn, M. J. Jang, H. Y. Um, B. J. Lee and H. S. Kim, *Acta Mater.*, 2018, **161**, 388–399.

19 J. W. Bae and H. S. Kim, *Scr. Mater.*, 2020, **186**, 169–173.

20 B. Zhang, X. Zheng, O. Voznyy, R. Comin, M. Bajdich, M. Garcia-Melchor, L. Han, J. Xu, M. Liu, L. Zheng, F. P. G. de Arquer, C. T. Dinh, F. Fan, M. Yuan, E. Yassitepe, N. Chen, T. Regier, P. Liu, Y. Li, P. De Luna, A. Janmohamed, H. L. Xin, H. Yang, A. Vojvodic and E. H. Sargent, *Science*, 2016, **352**, 333–337.

21 D. Gao, W. Zhu, J. Chen, K. Qin, M. Ma, J. Shi, Q. Wang, Z. Fan, Q. Shao, F. Liao, M. Shao and Z. Kang, *ACS Catal.*, 2024, **14**, 3700–3711.

22 L. Zhang, H. Wei, H. Li, Z. Su and X. Gong, *Int. J. Hydrogen Energy*, 2023, **48**, 25390–25397.

23 S. Chen, H. Huang, P. Jiang, K. Yang, J. Diao, S. Gong, S. Liu, M. Huang, H. Wang and Q. Chen, *ACS Catal.*, 2020, **10**, 332–336.

24 A. Zagalskaya and V. Alexandrov, *ACS Catal.*, 2020, **10**, 3650–3657.

25 K. Liu, C. Shi, J. Yu, E. Zhu, Z. Li, C. Zhang, W. Li, X. Yang, Y. Zhang and M. Xu, *Int. J. Hydrogen Energy*, 2021, **46**, 28011–28020.

26 A.-L. Wang, H. Xu and G.-R. Li, *ACS Energy Lett.*, 2016, **1**, 445–453.

27 M. Yang, M. Zhao, J. Yuan, J. Luo, J. Zhang, Z. Lu, D. Chen, X. Fu, L. Wang and C. Liu, *Small*, 2022, **18**, 2106554.

28 C. Wu, H. Li, Z. Xia, X. Zhang, R. Deng, S. Wang and G. Sun, *ACS Catal.*, 2020, **10**, 11127–11135.

29 Y.-Y. Ma, Z.-L. Lang, L.-K. Yan, Y.-H. Wang, H.-Q. Tan, K. Feng, Y.-J. Xia, J. Zhong, Y. Liu, Z.-H. Kang and Y.-G. Li, *Energy Environ. Sci.*, 2018, **11**, 2114–2123.

30 H. Sun, C. Tian, G. Fan, J. Qi, Z. Liu, Z. Yan, F. Cheng, J. Chen, C.-P. Li and M. Du, *Adv. Funct. Mater.*, 2020, **30**, 1910596.

31 Y. Duan, L. Yang, J. Gao, S. Guo, M. Hou, T. Hu and J. Qiu, *Arabian J. Sci. Eng.*, 2020, **45**, 4809–4816.

32 H. Bian, R. Wang, K. Zhang, H. Zheng, M. Wen, Z. Li, Z. Li, G. Wang, G. Xie, X. Liu and L. Jiang, *Surf. Coat. Technol.*, 2023, **459**, 129407.

33 S. Xin, Y. Tang, B. Jia, Z. Zhang, C. Li, R. Bao, C. Li, J. Yi, J. Wang and T. Ma, *Adv. Funct. Mater.*, 2023, **33**, 2305243.

34 M. B. Stevens, L. J. Enman, E. H. Korkus, J. Zaffran, C. D. M. Trang, J. Asbury, M. G. Kast, M. C. Toroker and S. W. Boettcher, *Nano Res.*, 2019, **12**, 2288–2295.

35 Q. Qi, C. Zhang and J. Hu, *Coord. Chem. Rev.*, 2025, **522**, 216235.

36 C. Zhou, X. Han, F. Zhu, X. Zhang, Y. Lu, J. Lang, X. Cao and H. Gu, *Int. J. Hydrogen Energy*, 2022, **47**, 27775–27786.

37 X. Gong, H. Zhong, L. A. Estudillo-Wong, N. Alonso-Vante, Y. Feng and D. Li, *J. Energy Chem.*, 2022, **74**, 376–386.

38 Y. Liu, X. Wang, M. Yang, Y. Li, Y. Xiao and J. Zhao, *Nanoscale*, 2023, **15**, 17936–17945.